MAGNETICALLY DRIVEN ACCRETION FLOWS IN THE KERR METRIC. I. MODELS AND OVERALL STRUCTURE

JEAN-PIERRE DE VILLIERS AND JOHN F. HAWLEY

Department of Astronomy, University of Virginia, P.O. Box 3818, University Station, Charlottesville, VA 22903-0818;
jd5v@virginia.edu; jh8h@virginia.edu

AND

JULIAN H. KROLIK

Department of Physics and Astronomy, Johns Hopkins University, 3400 North Charles Street, Baltimore, MD 21218-2686;
jhk@pha.jhu.edu

ABSTRACT

This is the first in a series of papers that investigate the properties of accretion flows in the Kerr metric through three-dimensional general relativistic magnetohydrodynamic simulations of tori with a nearly Keplerian initial angular velocity profile. We study four models with increasing black hole spin, from $a/M = 0$ to 0.998, for which the structural parameters of the initial tori are maintained nearly constant. The subsequent accretion flows arise self-consistently from stresses and turbulence created by the magnetorotational instability. We investigate the overall evolution and the late-time global structure in the resulting nonradiative accretion flows, including the magnetic fields within the disks, the properties of the flow in the plunging region, and the flux of conserved quantities into the black hole. Independent of black hole spin, the global structure is described in terms of five regions: the main disk body, the coronal envelope, the inner disk (consisting of an inner torus and plunging region), an evacuated axial funnel, and a biconical outflow confined to the corona-funnel boundary. We find evidence for lower accretion rates, stronger funnel-wall outflows, and increased stress in the near-hole region with increasing black hole spin.

Subject headings: accretion, accretion disks — black hole physics — instabilities — MHD

1. INTRODUCTION

With the recognition that the magnetorotational instability (MRI; Balbus & Hawley 1991, 1998) drives disk turbulence and the outward transport of angular momentum, the theory of black hole accretion is moving from relatively simple parameterized, one-dimensional, and time-independent models toward genuine dynamics. Because of the complexity of the underlying physics, however, large-scale computer simulations are essential. With the ever increasing power of computers, such simulations are now possible, and their realism should rapidly improve. The goal is increasingly detailed and predictive theoretical models to compare with and provide interpretation for observations.

Until recently, most simulations of accretion flows were carried out using Newtonian gravity or a pseudo-Newtonian approximation to the Schwarzschild potential. In particular, a number of pseudo-Newtonian simulations have focused on the inner edge of an accretion disk orbiting a black hole (Hawley & Krolik 2001, 2002, hereafter HK01, HK02, respectively; Armitage, Reynolds, & Chiang 2001; Armitage & Reynolds 2003; Machida & Matsumoto 2003). The dynamical behavior of the inner edge is critical in determining the efficiency of accretion, as well as the energy and angular momentum carried into the hole. Recent analytic work (Krolik 1999; Gammie 1999) and numerical studies have found that, in contrast to the conventional picture, magnetic stress can operate on the flow within the last stable orbit, increasing the nominal efficiency of the accretion and delivering less specific angular momentum to the hole. Simulations have also shown that the turbulence in the disk is marked by rapid and large amplitude fluctuations, result-

ing in a highly nonsteady accretion rate. The implications of these results for black hole accretion disks were summarized by Krolik & Hawley (2002, hereafter KH02), who identified several distinct functional definitions of the inner edge of an accretion disk.

While the general properties of an accretion disk around a Schwarzschild black hole may be modeled reasonably well by a pseudo-Newtonian potential, many of the important features of the inner edge of disks depend strongly on the spin of the black hole, characterized by the parameter a/M. Since it is hoped that observable accretion diagnostics may provide a means to measure a/M in black hole systems, it is essential to understand the specific effects of black hole spin, and this requires simulations using full relativity. In this study, we model accretion flows by using ideal general relativistic magnetohydrodynamics (GRMHD) in the stationary background of a Kerr black hole with the recently developed code of De Villiers & Hawley (2003a, hereafter DH03a).

In an earlier paper, De Villiers & Hawley (2003b, hereafter DH03b) presented an initial survey of the properties of accretion tori in the Kerr metric at moderate resolution. These first simulations used constant specific angular momentum (constant l) tori threaded by poloidal loops of magnetic field as the initial state. These simulations demonstrated similarities between accretion into a Schwarzschild hole and earlier pseudo-Newtonian simulations of Hawley (2000, hereafter H00), while explicitly highlighting the differences that result from the Kerr metric. The effect of frame dragging was observed, especially in the retrograde torus, where it caused a reversal of flow direction in the inspiraling accretion stream. The black hole spin determines the

location of the marginally stable orbit, which, in turn, strongly affects the innermost regions of the flow. A constant angular momentum torus is a particularly short-lived configuration in the presence of the MRI, and its initial evolution includes a violent transient accretion phase as the disk readjusts to a more nearly Keplerian angular momentum distribution. After this, the disk models settled into a state of sustained turbulence with an accretion rate that decreased with increasing a/M. In all models, the magnetic pressure became strong in the near-hole region, with a late-time magnetic pressure comparable to the initial gas pressure maximum in the torus.

In this paper, we pick up the thread of HK01 and HK02 and present the results of a series of high-resolution simulations of nonradiative accretion flows in the Kerr metric. We revisit the initial state of model GT4 originally investigated in H00 and subsequently the focus of HK01 and HK02, which features an initial angular momentum distribution with a radial dependence that is slightly shallower than Keplerian. The torus is seeded with loops of weak poloidal magnetic field. As in the earlier nonrelativistic studies, we pay particular attention to the inner region of the accretion disk since the most extreme relativistic effects and the greatest energy release happen near the radius of the marginally stable orbit, r_{ms}. In the near-hole region, an accretion flow must make a transition from strong turbulence within the disk to a more nearly laminar flow as matter plunges toward the black hole, and simulations find that the location of this transition is highly time variable. Generally the transition begins outside r_{ms}, but the transonic plunging inflow is not fully established until some point inside r_{ms}. The inner disk edge is not abrupt: average flow variables, including the stress, are relatively smooth, albeit time-varying, functions of radius. Magnetic stress continues to be important even within the plunging region. In fact, the magnetic stress becomes proportionally more important as flux freezing increases the field strength relative to the gas pressure (Krolik 1999) and increases the correlation between the radial and azimuthal field components.

This paper is the first in a series that investigates in detail a coherent set of accretion disk simulations. Here we introduce the basic models and present a preliminary analysis of the results. In § 2 we describe the analytic expressions that are used to initialize the models, and the parameters of the four models studied. We also list a number of the physics diagnostics used in the simulations. In § 3 we present an overview of results of the three-dimensional global MHD simulations, focusing on the broad evolutionary features and aspects that are common to all four models. We examine some of the late-time properties of the disks, highlighting the key features through a structural classification of the accretion system. In this classification, we distinguish five main regions: the main disk body, the coronal envelope, the inner disk, the funnel-wall jet, and the axial funnel. In § 4 we review and summarize our findings. In the course of the presentation and analysis of results, we pose some of the questions that will be the subject of subsequent investigations.

2. NUMERICAL APPROACH AND INITIAL CONDITIONS

We use a finite difference code to solve the equations of ideal GRMHD in the spacetime of a Kerr (rotating) black hole. We adopt the familiar Boyer-Lindquist coordinates, (t, r, θ, ϕ), for which the line element has the form

$$ds^2 = \mathbf{g}_{tt}dt^2 + 2\mathbf{g}_{t\phi}dtd\phi + \mathbf{g}_{rr}dr^2 + \mathbf{g}_{\theta\theta}d\theta^2 + \mathbf{g}_{\phi\phi}d\phi^2 \ . \quad (1)$$

We use the metric signature $(-, +, +, +)$, along with geometrodynamic units where $G = c = 1$. Time and distance are in units of the black hole mass, M. The determinant of the four-metric is g, and $\sqrt{-g} = \alpha\sqrt{\gamma}$, where α is the lapse function, $\alpha = 1/\sqrt{-\mathbf{g}^{tt}}$, and γ is the determinant of the spatial three-metric. We follow the usual convention of using Greek characters to denote full spacetime indices and Roman characters for purely spatial indices.

The equations of ideal GRMHD are the law of baryon conservation, $\mathbf{V}_\mu(\rho U^\mu) = 0$, where $\mathbf{V}_\mu$ is the covariant derivative; the conservation of stress-energy, $\mathbf{V}_\mu \mathbf{T}^{\mu\nu} = 0$, where $\mathbf{T}^{\mu\nu}$ is the energy-momentum tensor for the fluid; and the induction equation, $\mathbf{V}_\mu{}^*\mathbf{F}^{\mu\nu} = 0$, where ${}^*\mathbf{F}^{\mu\nu}$ is the dual of the electromagnetic field strength tensor. The precise form of the equations that are solved in the code is derived in DH03a, along with a set of primary and secondary variables especially suited to numerical evolution. A succinct presentation of the equations is provided in DH03b and will not be repeated here, although for reference we reiterate the definitions of the primary code variables.

The state of the relativistic test fluid at each point in the spacetime is described by its density ρ, specific internal energy ϵ, four-velocity U^μ, and isotropic pressure P. The relativistic enthalpy is $h = 1 + \epsilon + P/\rho$. The pressure is related to ρ and ϵ through the equation of state of an ideal gas, $P = \rho\epsilon(\Gamma - 1)$, where Γ is the adiabatic exponent. For these simulations we take $\Gamma = 5/3$. The entropy of the gas can increase in regions of strong compression (shocks), through the action of an artificial viscosity.

The magnetic field of the fluid is described by two sets of variables, the constrained transport magnetic field, $\mathbf{F}_{jk} = \mathscr{B}^i$, and the magnetic field four-vector $\sqrt{4\pi}b^\mu = \mathbf{F}^{\mu\nu}U_\nu$. The ideal MHD condition requires $U^\nu \mathbf{F}_{\mu\nu} = 0$. The magnetic field b^μ is included in the definition of the total four-momentum,

$$\mathbf{S}_\mu = (\rho h + \| b \|^2)W U_\mu \ , \quad (2)$$

where W is the boost factor. We define auxiliary density and energy functions $D = \rho W$ and $E = D\epsilon$, respectively, and transport velocity $V^i = U^i/U^t$. We also define the specific angular momentum as $l = -U_\phi/U_t$, and the angular velocity as $\Omega = U^\phi/U^t$. The numerical scheme is built on the set of variables $D, E, \mathbf{S}_\mu, V^i, \mathscr{B}^i$, and b^μ.

2.1. Torus Initial State

For consistency with past studies we choose as our initial condition a somewhat thick torus with a nearly Keplerian distribution of angular momentum, specifically a general relativistic version of the GT4 model of H00. To create such a model we follow the procedure described by Chakrabarti (1985) to construct equilibria with nonconstant angular momentum distributions in the Kerr metric. We seek a solution in which the disk has a power-law rotation,

$$\Omega = \eta\lambda^{-q} \ , \quad (3)$$

where η is a constant, q is a positive number, and λ is given

by

$$\lambda^2 = \frac{l}{\Omega} = l\,\frac{\mathbf{g}^{tt} - l\mathbf{g}^{t\phi}}{\mathbf{g}^{t\phi} - l\mathbf{g}^{\phi\phi}}\;. \tag{4}$$

In the Schwarzschild metric, this parameter has the form $\lambda^2 = -\mathbf{g}^{tt}/\mathbf{g}^{\phi\phi}$. In Newtonian gravity λ is simply the cylindrical radius.

In the hydrodynamic limit, the momentum evolution equation is

$$\partial_t(\mathbf{S}_j) + \frac{1}{\sqrt{\gamma}}\partial_i\sqrt{\gamma}(\mathbf{S}_j\mathbf{V}^i) + \frac{1}{2}\left(\frac{\mathbf{S}_\epsilon\mathbf{S}_\mu}{\mathbf{S}^t}\right)\partial_j\mathbf{g}^{\mu\epsilon} + \alpha\partial_j(P) = 0\;, \tag{5}$$

where $\mathbf{S}_j = \rho h W \mathbf{U}_j$ is the momentum, and the other variables are defined as above (Hawley, Smarr, & Wilson 1984). The momentum equation is simplified by imposing time independence and axisymmetry and requiring that there be no poloidal motion. This simplified equation reads

$$\alpha\partial_j(P) + \frac{1}{2}\frac{\mathbf{S}_\epsilon\mathbf{S}_\mu}{\mathbf{S}^t}\partial_j\mathbf{g}^{\mu\epsilon} = 0\;. \tag{6}$$

Using the definition of the momentum four-vector and the definition of specific angular momentum, we obtain

$$\frac{\partial_j(P)}{\rho h} = -\frac{\mathbf{U}_t^2}{2}\partial_j(\mathbf{U}_t^{-2}) + \mathbf{U}_t^2(-\partial_j\mathbf{g}^{t\phi} + l\partial_j\mathbf{g}^{t\phi})\partial_j l\;, \tag{7}$$

where $\mathbf{U}_t^{-2} = \mathbf{g}^{tt} - 2l\mathbf{g}^{t\phi} + l^2\mathbf{g}^{\phi\phi}$, a result which follows from $\mathbf{U}_\mu\mathbf{U}^\mu = -1$ and $\mathbf{U}_r = \mathbf{U}_\theta = 0$.

Under the assumption of constant entropy, $Tds = 0$, we use $dh = dp/\rho$ to write

$$\frac{\partial_j h}{h} = -\frac{1}{2}\frac{\partial_j(\mathbf{U}_t^{-2})}{\mathbf{U}_t^{-2}} + \mathbf{U}_t^2(-\partial_j\mathbf{g}^{t\phi} + l\partial_j\mathbf{g}^{t\phi})\partial_j l\;. \tag{8}$$

To integrate this equation, we assume that $\Omega \equiv \Omega(l)$ and use the definition of $\mathbf{U}_t$ above, along with the relation $\Omega = (\mathbf{g}^{t\phi} - l\mathbf{g}^{\phi\phi})/(\mathbf{g}^{tt} - l\mathbf{g}^{t\phi})$ to get

$$\frac{\partial_j h}{h} = -\frac{1}{2}\frac{\partial_j(\mathbf{U}_t^{-2})}{\mathbf{U}_t^{-2}} + \frac{\Omega}{1 - l\Omega}\partial_j l\;. \tag{9}$$

[As pointed out by Abramowicz, Jaroszyński, & Sikora 1978, $-\mathbf{U}_t(r,\,\theta;\,l)$ plays a role analogous to an effective potential.] To find a disk solution, we use equation (3) and the definition of λ to write $l = \Omega\lambda^2 = \eta\lambda^{2-q}$ and $\Omega = \eta^{-2/(q-2)}l^{q/(q-2)} \equiv kl^\alpha$. So,

$$\int_{h_{\rm in}}^h \frac{dh}{h} = -\frac{1}{2}\int_{U_{\rm in}}^{U_t} \frac{d(\mathbf{U}_t^{-2})}{\mathbf{U}_t^{-2}} + \int_{l_{\rm in}}^l \frac{kl^\alpha}{1 - kl^{\alpha+1}}\,dl\;, \tag{10}$$

where $\alpha = q/(q-2)$ and $x_{\rm in}$ refers to the quantity in question evaluated on the surface of the disk. Clearly, $h_{\rm in} = 0$, and a general solution admitting a choice of surface binding energy $\mathbf{U}_{\rm in}$ is given by

$$h(r,\,\theta) = \frac{\mathbf{U}_{\rm in}f(l_{\rm in})}{\mathbf{U}_t(r,\,\theta)f(l(r,\,\theta))}\;, \tag{11}$$

where

$$f(l) = \left\|1 - kl^{\alpha+1}\right\|^{1/(\alpha+1)}$$

or

$$f(\Omega) = \left\|1 - k^{-1/\alpha}\Omega^{(\alpha+1)/\alpha}\right\|^{1/(\alpha+1)}\;.$$

Using the equation of state and the definition of enthalpy, the internal energy of the disk is

$$\epsilon(r,\,\theta) = \frac{1}{\Gamma}\left\{\frac{\mathbf{U}_{\rm in}f(l_{\rm in})}{\mathbf{U}_t(r,\,\theta)f(l(r,\,\theta))} - 1\right\}\;. \tag{12}$$

For a constant-entropy adiabatic gas the pressure is given by $P = \rho\epsilon(\Gamma - 1) = K\rho^\Gamma$, and the density is given by $\rho = [\epsilon(\Gamma - 1)/K]^{1/(\Gamma-1)}$.

For the Schwarzschild metric, these analytic relations completely specify the initial equilibrium torus. In the Kerr metric, λ^2 is an implicit function of l, requiring an iterative procedure to solve for the equilibrium state. However, it is not essential to construct a torus that is in strict hydrostatic equilibrium. It is sufficient to use the Schwarzschild expression for λ to initialize an approximate equilibrium for a torus orbiting a Kerr hole. The differences between even an extreme Kerr and a Schwarzschild metric are relatively small at the location of the initial pressure maximum for the tori of interest here. In addition, we introduce a seed magnetic field and ignore its contribution to the equilibrium solution, which is also a satisfactory approximation as long as the imposed field is weak. In the final analysis, motions resulting from the MRI quickly dominate the evolution regardless.

A particular disk solution is specified by choosing the parameter q, the entropy parameter K, and the angular momentum $l_{\rm in}$ at $r_{\rm in}$, the inner edge of the disk. For all simulations, the location of the inner edge, as well as the parameters $K = 0.01$ and $q = 1.68$, are kept fixed. The specific angular momentum $l_{\rm in}$ is chosen to maintain the location of the pressure maximum constant for all values of the Kerr parameter a/M.

The initial magnetic field is obtained from the definition of $\mathbf{F}_{\mu\nu}$ in terms of the four-vector potential, A_μ, $\mathbf{F}_{\mu\nu} = \partial_\mu A_\nu - \partial_\nu A_\mu$. Our initial field consists of axisymmetric poloidal field loops, laid down along isodensity surfaces within the torus by defining $A_\mu = (A_t,\,0,\,0,\,A_\phi)$, where

$$A_\phi = \begin{cases} k(\rho - \rho_{\rm cut}) & \text{for } \rho \geq \rho_{\rm cut}\,, \\ 0 & \text{for } \rho < \rho_{\rm cut}\,, \end{cases} \tag{13}$$

where $\rho_{\rm cut}$ is a cutoff density corresponding to a particular isodensity surface within the torus. Using the above definition, it follows that $\mathcal{B}^r = -\partial_\theta A_\phi$ and $\mathcal{B}^\theta = \partial_r A_\phi$. The constant k is set by the input parameter β, the ratio of the gas pressure to the magnetic pressure, using the volume-integrated gas pressure divided by the volume-integrated magnetic energy density in the initial torus. We use $\beta = 100$ in all runs except for one model (KDP), which instead uses $\beta = 200$. The constant $\rho_{\rm cut}$ is chosen to keep the initial magnetic field away from the outer edge of the disk. Here we use $\rho_{\rm cut} = 0.5\rho_{\rm max}$, where $\rho_{\rm max}$ is the maximum density at the center of the torus, to ensure that the initial field loops are confined well inside the torus.

The region outside the torus is initialized to a numerical vacuum that consists of a cold, tenuous, nonrotating, unmagnetized gas. The auxiliary density variable, D, in the vacuum is set to 7 orders of magnitude below the maximum value of D in the initial torus. Similarly, the auxiliary energy variable E is set 14 orders of magnitude below the initial

maximum of E. These values define the numerical floor of the code, below which D and E are not allowed to drop. In practice, the numerical floor is rarely applied during a simulation, since outflow from the evolving torus quickly populates the grid with a gas that, although of low density, lies above the numerical floor. Further details on the numerical floor are given in DH03a and DH03b.

2.2. Overview of Torus Models

In this series of simulations we concentrate on the effect of different black hole spin parameters on the evolution of similar initial torus models. We consider a torus orbiting a Schwarzschild black hole and tori orbiting prograde Kerr holes with values $a/M = 0.5$, 0.9, and 0.998. These models are designated KD0 (Kepler disk, 0 black hole spin), KDI (intermediate spin), KDP (strong prograde spin), and KDE (extreme spin), respectively. We choose parameters for the initial tori that keep the inner edge of the disk and the location of the initial pressure maximum constant as the black hole rotation parameter is varied. Table 1 lists the general properties of the models, where l_{in} denotes the specific angular momentum at r_{in}, the inner edge of the disk (in the equatorial plane), $(-U_t)_{in}$ is the energy per unit mass of matter at the surface of the torus, $r_{P\max}$ is the location of the pressure maximum (also in the equatorial plane), and $\mathbf{T}_{orb}$ is the orbital period at the pressure maximum in units of M. For reference we also list r_{ms}, the location of the marginally stable orbit, the values of $(U_\phi)_{ms}$ and $(U_t)_{ms}$ for a particle in a circular orbit at r_{ms} (Bardeen, Press, & Teukolsky 1972), and $\mathbf{T}_{orb(ms)}$ the orbital period of a test particle at the marginally stable orbit in units of M. All radii in the table are in units of M. Note that the quantity $\mathbf{T}_{orb}$ evaluated at the pressure maximum is used in the following sections as the unit of the evolution time of the simulations.

Both moderate- and high-resolution simulations were carried out for these models. The lower resolution simulations use a $128 \times 128 \times 32$ grid in (r, θ, ϕ); these models are indicated with an "lr" appended to their names, e.g., KD0lr. The high-resolution simulations use a $192 \times 192 \times 64$ grid. The azimuthal grid spans the quarter plane, $0 \le \phi \le \pi/2$, with periodic boundary conditions in ϕ. The use of a restricted azimuthal domain significantly reduces the total computational time required for a given grid zone size, $\Delta\phi$. The drawback is that long-wavelength, low azimuthal wavenumber m-modes cannot be represented. DH03b ran a comparison between a partial and a full 2π grid and found that the overall dynamical behavior of the accretion flow was unchanged with the restricted azimuthal domain. The full 2π model did have reduced time variability in the accretion rate, and 6% greater mass accretion into the hole, with comparable increases in stress and magnetic energy. This result is consistent with previous Newtonian and pseudo-Newtonian tests (Hawley 2001;

Steinacker & Papaloizou 2002; Papaloizou & Nelson 2003) that found quantitative differences at the 10% level or below. The θ-grid ranges over $0.045\pi \le \theta \le 0.955\pi$, with an exponential grid spacing function that concentrates zones near the equator. Reflecting boundary conditions are enforced in the θ-direction. The outer radial boundary is set to $r_{\max} = 120M$ in all cases; the inner radial boundary is located just outside the horizon, with the specific value depending on the location of the horizon as determined by the Kerr spin parameter a/M. The inner boundary is at $r_{\min} = 2.05M$, $1.90M$, $1.45M$, and $1.175M$ for models KD0, KDI, KDP, and KDE, respectively. The radial grid is set using a hyperbolic cosine function to maximize the resolution near the inner boundary. The hyperbolic cosine function ensures that there is a tighter grid spacing (Δr_i) near the inner boundary than would be provided by the exponential spacing in traditional "logarithmic" grids. This type of grid ensures that the plunging region is well resolved in the KD0, KDI, and KDP models and marginally so in model KDE, in which this region occupies a very small range of radii near the inner boundary. Boundary values are obtained for all variables, including magnetic fields, by extrapolation into the boundary with a slope of zero. To prevent flow from the boundaries onto the grid, the radial momentum, S_r, is set to zero in the ghost zones if the flow direction would otherwise be onto the grid. The boundary values for the transport velocities, V^i, are constructed from the boundary momenta by using the usual momentum normalization procedure (DH03a).

Figure 1 shows the initial density profiles for these tori, plotted on the same spatial scale to illustrate clearly the relative size of the disks. The color map saturates in the vacuum region surrounding the disk, where the density (ρ) is 7 orders of magnitude below $\rho_{\max}$. Note that choosing to fix the inner edge and pressure maximum locations in the tori means that the greater the spin parameter, the larger the torus. Overlaid on the tori are contours of the initial magnetic pressure plotted on a logarithmic scale. The choice of vector potential density cutoff (eq. [13]), $\rho_{cut} = 0.5\rho_{\max}$, yields initial poloidal loops concentrated around the pressure maximum and fully contained within the torus. The chevron-shaped magnetic pressure contour lines show that the magnetic pressure is largest inside $r_{P\max}$. The field in this region is rapidly amplified by shear, and this contributes to the expulsion of a thin stream of magnetized gas through the inner edge of the disk during the first orbit.

2.3. Evolution Diagnostics

Full three-dimensional time-dependent simulations can generate an enormous amount of data. To handle this data, we have developed a variety of evolution diagnostics designed to organize and analyze the results. First, complete dumps of the code variables are saved at periodic intervals,

TABLE 1
GLOBAL TORUS SIMULATION PARAMETERS

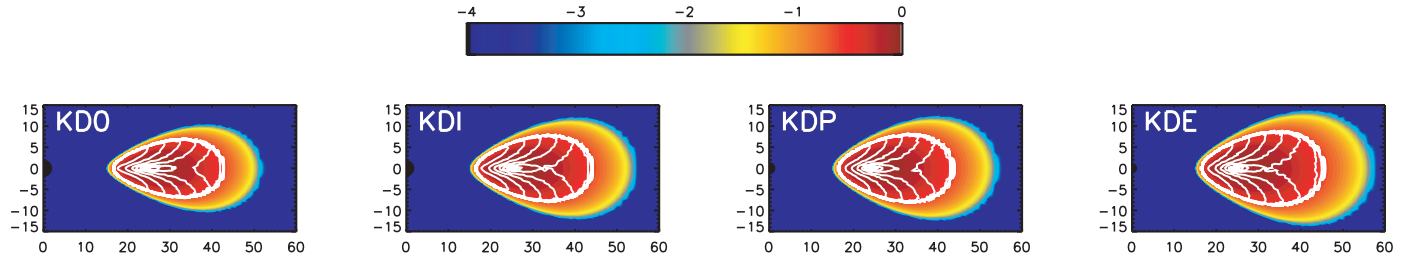| Model	a/M	β	l_{in}	$(U_t)_{in}$	r_{in}	$r_{P\max}$	$\mathbf{T}_{orb}$	r_{ms}	$(U_\phi)_{ms}$	$(U_t)_{ms}$	$\mathbf{T}_{orb(ms)}$
KD0	0.000	100	4.66	−0.9725	15.0	25.0	785	6.00	3.464	−0.943	97.95
KDI	0.500	100	4.61	−0.9730	15.0	25.0	794	4.23	2.903	−0.918	62.57
KDP	0.900	200	4.57	−0.9732	15.0	25.0	803	2.32	2.100	−0.844	31.04
KDE	0.998	100	4.57	−0.9734	15.0	25.0	803	1.23	1.392	−0.679	15.73

Fig. 1.—Initial density (ρ) and magnetic pressure ($\|b\|^2/2$) profiles for the KD0, KDI, KDP, and KDE models. Density is scaled logarithmically in relation to the maximum, as shown in the color bar. The magnetic pressure, shown as 10 overlaid contour lines, is also scaled logarithmically over 4 decades from the pressure maximum. The individual plots are labeled by model.

and these can be examined in detail after a simulation. For these models such dumps are saved every $80M$ in time; this represents 10 dumps per orbital period at $r_{P\,\mathrm{max}}$ or, equivalently, 0.2–1.2 dumps per orbital period at r_{ms}, depending on a/M. In addition, we save the density variable every $2M$ in time to produce high time resolution animations. We also compute a more extensive set of azimuthally averaged variables, variables averaged on spherical shells, and volume-integrated quantities. These are saved every $1M$ of time. All these data are archived and serve as a resource for more detailed studies in subsequent work.

At each radius we define the shell-averaged quantity, $\mathscr{X}$, as

$$\langle \mathscr{X} \rangle(r) = \frac{1}{\mathscr{A}(r)} \iint \mathscr{X} \sqrt{-g}\, d\theta\, d\phi , \qquad (14)$$

where the area of a shell is $\mathscr{A}(r)$ and the bounds of integration range over the full range of the θ and ϕ coordinates in the computational domain. For these simulations we compute shell-averaged values of density, $\langle \rho \rangle$, density-weighted angular momentum, $\langle \rho l \rangle$, gas pressure, $\langle P \rangle$, magnetic field strength $\langle \|b\|^2 \rangle$, canonical angular momentum density $\langle \rho h U_\phi \rangle$, and energy density $\langle -\rho h U_t \rangle$. From these we derive quantities such as the density-weighted average specific angular momentum, $\langle l \rangle = \langle \rho l \rangle / \langle \rho \rangle$.

Fluxes through the shell are computed in a similar manner, but are not normalized with the area. We evaluate the rest-mass flux $\langle \rho U^r \rangle$, energy flux

$$\langle \mathbf{T}^r_t \rangle = \langle \rho h U^r U_t \rangle + \langle \|b\|^2 U^r U_t \rangle - \langle b^r b_t \rangle , \qquad (15)$$

and the angular momentum flux

$$\langle \mathbf{T}^r_\phi \rangle = \langle \rho h U^r U_\phi \rangle + \langle \|b\|^2 U^r U_\phi \rangle - \langle b^r b_\phi \rangle . \qquad (16)$$

To provide flexibility in analysis, each of the three components in the above sums is calculated and stored separately. Again, various quantities can be subsequently derived from these fluxes and shell averages.

Volume-integrated quantities are computed using

$$[\mathscr{Q}] = \iiint \mathscr{Q} \sqrt{-g}\, dr\, d\theta\, d\phi . \qquad (17)$$

The volume-integrated quantities computed and saved as a function of time are the total rest mass, $[\rho U^t]$, angular momentum $[\mathbf{T}^t_\phi]$, and total energy $[\mathbf{T}^t_t]$.

These diagnostic calculations can be used to monitor the conservation of rest mass, energy, and momentum during the numerical evolution. Since the numerical grid is finite in

extent, the conservation laws, when written in integral form (Page & Thorne 1974), yield volume and surface terms that can be evaluated as described above. Within the limits of sampling frequency, it is possible to account for change in the total mass, energy, and angular momentum in terms of the net fluxes that leave the grid. Specifically, for the integrated quantities $[\mathscr{Q}]$, we monitor the corresponding cumulative flux through the inner and outer radial boundaries,

$$\{\mathscr{F}\}_{\mathrm{in,out}} = \int dt\, \langle \mathscr{F} \rangle(r_{\mathrm{in,out}}) . \qquad (18)$$

The history sum for rest-mass conservation is

$$M_{\mathrm{tot}} = [\rho U^t] + \{\rho U^r\}_{\mathrm{in}} + \{\rho U^r\}_{\mathrm{out}} ; \qquad (19)$$

for energy conservation, it is

$$E_{\mathrm{tot}} = [\mathbf{T}^t_t] + \{\mathbf{T}^r_t\}_{\mathrm{in}} + \{\mathbf{T}^r_t\}_{\mathrm{out}} ; \qquad (20)$$

and for momentum conservation (ϕ-component), it is

$$L_{\mathrm{tot}} = [\mathbf{T}^t_\phi] + \{\mathbf{T}^r_\phi\}_{\mathrm{in}} + \{\mathbf{T}^r_\phi\}_{\mathrm{out}} . \qquad (21)$$

3. SYNOPSIS OF RESULTS

The four models, KD0, KDI, KDP, and KDE, were evolved for a time equivalent to 10 orbits at their respective pressure maxima. Figure 2 shows polar and equatorial slices of the density (ρ) for model KDP at $t = 1.0$, 2.0, and 10.0 orbits; the figures for the other three models are comparable and are not shown. Overall, the general evolutionary phases identified in the constant angular momentum (SF) models of DH03b apply equally well to the evolution of the KD models: (1) the initial rapid growth of the toroidal magnetic field by shear; (2) the initial nonlinear saturation of the poloidal field MRI, which progresses outward through the torus; and (3) quasi-stationary evolution by sustained MHD turbulence in a disk with a roughly constant opening angle. However, there are also some differences between the two types of model. While the SF models experienced a violent transient prior to the onset of turbulence, there is no comparable event in the KD models. Instead, there is a gradual migration of a spiraling inflow toward the black hole (*left*), and the onset of the MRI occurs fairly quickly in the near-hole region, once the flow is established (*center*). This is because the growth rate of the MRI is proportional to Ω, which increases inward. The onset of the MRI then progresses gradually outward until the entire disk becomes turbulent. Another difference is that the SF models featured a violent expulsion of large buoyant magnetic bubbles, and
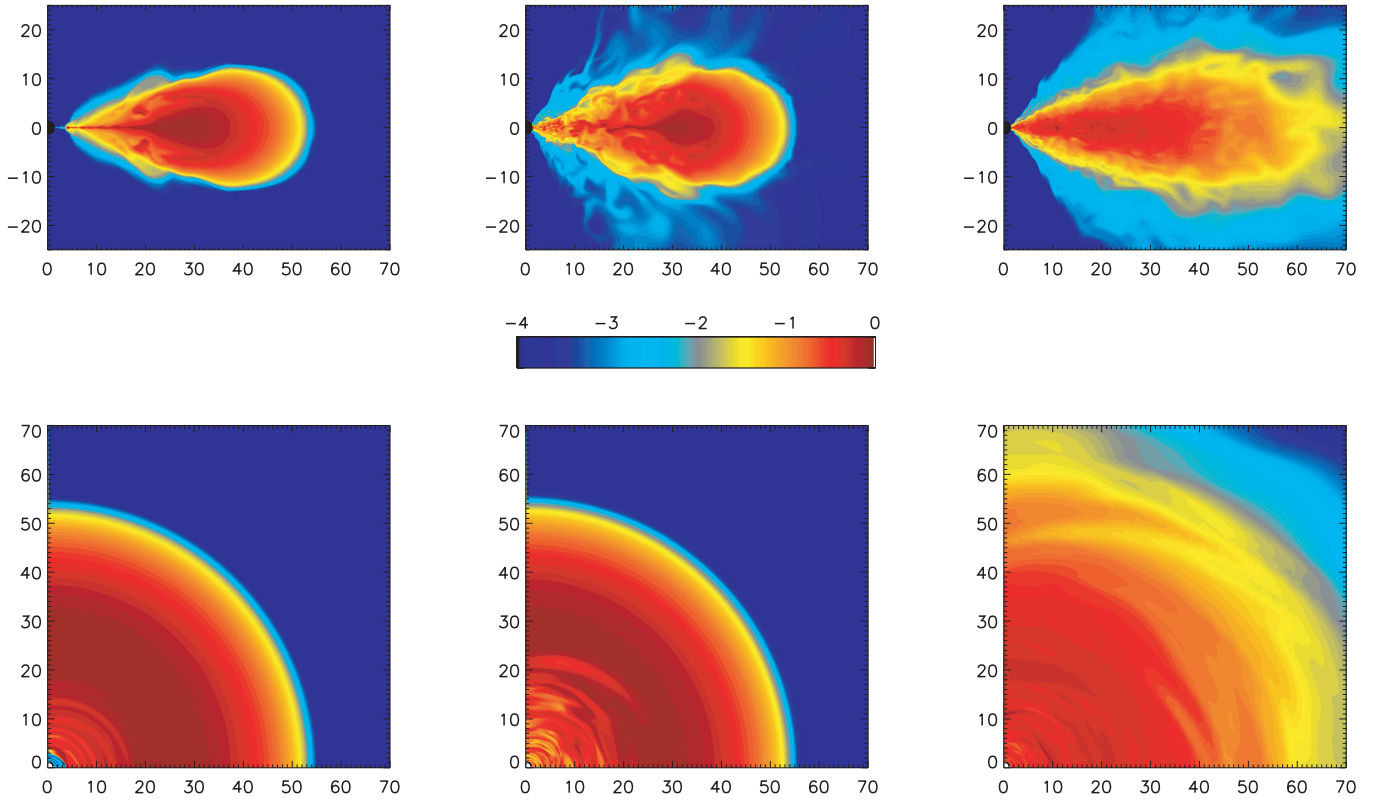
Fig. 2.—Plots of the logarithm of density (ρ) for model KDP. *Top*, Polar slices through the disk at $\phi = 0$; *bottom*, equatorial slices through the disk at $\theta = \pi/2$; *left*, at $t = 1.0$ orbits; *middle*, at $t = 2.0$ orbits; *right*, at $t = 10.0$ orbits.

such events are largely absent in the KD models. Instead, smaller scale low-density, high magnetic pressure regions can be seen moving outward along the surface of the disk (*top middle*). It is likely that the vigor of the early stages of the evolution in the SF tori derives from the much stronger inward-directed pressure gradient in the inner half of the torus. This pressure remains even after the MRI has cut the centrifugal support by reducing the super-Keplerian *l*-distribution to nearly Keplerian. The large buoyant magnetic bubbles in the SF models are the result of initial conditions; there is a relatively large amount of nonmagnetized gas surrounding the initial magnetized region inside the torus, and a substantial interchange instability feeds off this contrast as the field strengthens.

In the late stages of the evolution, all the KD models achieve a quasi–steady state with sustained turbulence. The general features observed in the four disk models are summarized in Figure 3, which shows the time and azimuthal average of the density over the 10th orbit of the KDP simulation. We distinguish five separate regions in the late-time flow: the main body of the disk; the coronal envelope; the inner disk, consisting of the inner torus and plunging region; the funnel-wall jet; and the axial funnel region. The overall characteristics of these regions are as follows:

1. The *main body of the disk* is a turbulent wedge of roughly constant opening angle containing most of the mass. The pressure scale height H at each radius can be measured by computing the point where the total pressure has fallen to e^{-1} of its value at the equator. Measured at $r = 20M$, $H/R \sim 0.18$ in model KD0,

$H/R \sim 0.2$ for models KDI and KDP, and $H/R \sim 0.25$ for model KDE. Inside $r = 20M$, H/R increases systematically with increasing a/M up to $H/R \sim 0.4$ for KDE. Inside the disk body gas pressure dominates ($\beta > 1$), and the magnetic and velocity fields are highly tangled. The outer part of the disk moves radially outward with time as it gains angular momentum.

2. The *coronal envelope* is a region of low density above the surface of the disk, where gas and magnetic pressure are comparable ($\beta \sim 1$). The magnetic field in this region is more regular than in the disk body. Animation sequences show an outflow driven from the inner region of the disk out along the surface of the disk. This outflow supplies gas and magnetic field to the coronal envelope.

3. The *inner torus and plunging region* are located at the inner edge of the accretion disk. The inner torus is a time-variable structure where matter accumulates from accretion from the main disk. It is marked by a local pressure and density maximum surrounded by a thickened disk. This region was referred to as the "minitorus" in DH03b and as the "inner torus" in the pseudo-Newtonian accretion simulation of Hawley & Balbus (2002, hereafter HB02); we adopt the latter term here. The density and pressure maximum is located just outside the marginally stable orbit; hence, the inner torus is found at smaller radii with increasing a/M. In the same way, the inner torus becomes denser (in relation to the initial density maximum) and hotter with increasing black hole spin. The density and pressure drop inside the inner torus as the disk approaches the plunging region where matter leaves the disk and spirals into the black hole. The plunging region begins near the marginally stable orbit.
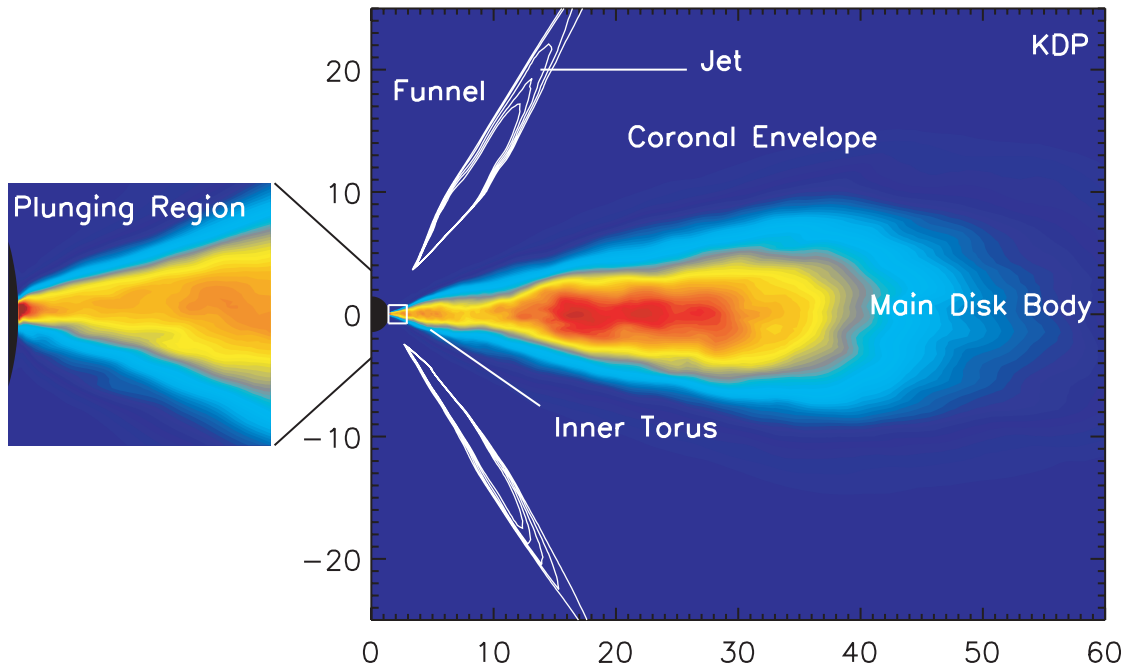
FIG. 3.—Azimuthally averaged density (ρ) time-averaged over the 10th orbit plotted on a linear scale for model KDP. The main dynamical features of the system are labeled. The jet is outlined by contours of positive radial momentum. The box on the left is a close-up showing the plunging region from just outside the marginally stable orbit to the black hole horizon. The labeled features are seen in all the simulations.

Here matter spirals in toward the event horizon, stretching field lines as it falls. Most of the matter in the inner torus eventually accretes into the black hole, but some is ejected into outflows in the coronal envelope and along the funnel wall.

4. The *funnel-wall jet* is an outflow along the centrifugal barrier that originates in the vicinity of the inner torus. The density in the jet is small compared with the disk but 1–2 orders of magnitude greater than in the funnel itself. The contours in Figure 3 that delineate the jet are selected positive values of the time and azimuthal average of radial momentum. The intensity of the jet is model dependent: the jet is weak in model KD0; there is progressively more outflow with increasing a/M.

5. The *axial funnel* is a magnetically dominated region in which there is very tenuous gas, several orders of magnitude below the density in the disk body. The small amount of gas in the funnel has negligible angular momentum. The funnel contains a predominantly radial magnetic field; the magnetic pressure near the hole is comparable to the maximum gas pressure in the initial torus. The funnel region is cleanly

separated from the coronal envelope by the centrifugal barrier.

The entire flow is characterized by large fluctuations in both space and time. In addition, animations of the simulation data show large-scale trailing spiral waves in all regions of the disk and coronal envelope. In the following sections we use this structural classification of the accretion system as a guide and expand on some of the properties, both structural and dynamical, of these regions.

3.1. *Main Disk Body*

The disk evolves from its initial state to its late-time quasi–steady state by redistributing angular momentum and spreading out radially in both directions. The evolution is clearly illustrated through a time series of shell-averaged densities, $\langle\rho\rangle(r)$, which are shown in Figure 4. These graphs capture the overall redistribution of mass while showing how the inner region of the accretion disk is established. The increase in maximum density and the inward migration
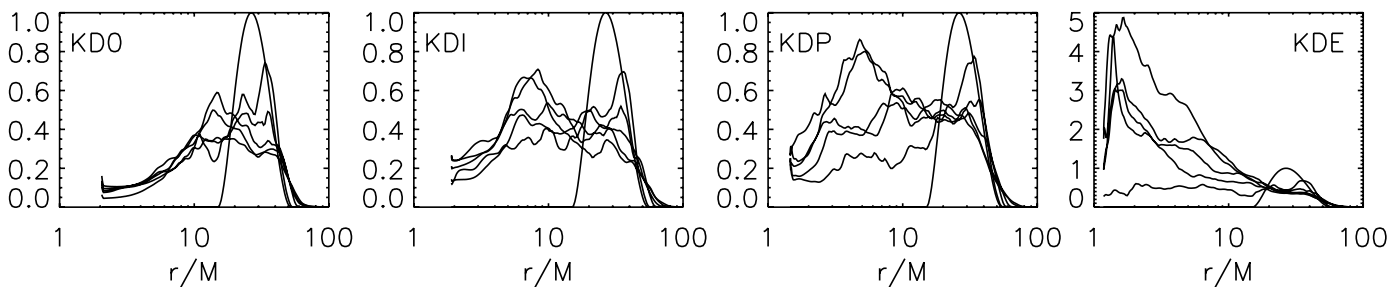

FIG. 4.—Sequence of density profiles $\langle\rho\rangle(r)$ for the high-resolution models at $t = 0$, 2, 4, 6, 8, and 10 orbits. Density is given in units of the initial density maximum, $\rho_{max}(t = 0)$. The thick lines correspond to the initial and final density profiles. The individual plots are labeled by model.
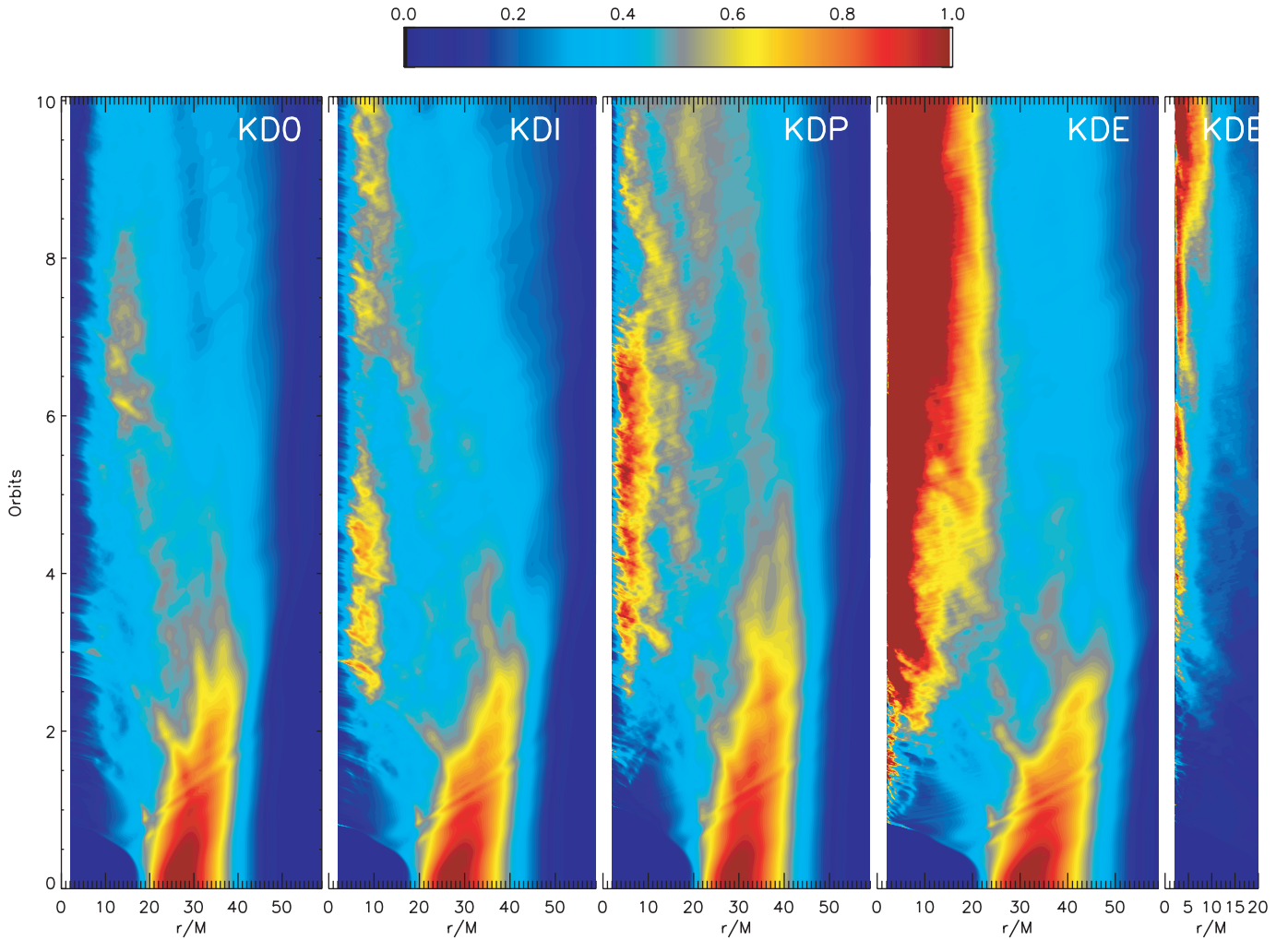
FIG. 5.—Spacetime diagrams of $\langle \rho \rangle (r, \, t)$ for high-resolution models KD0, KDI, KDP, and KDE. Density is plotted on a linear scale, in units of the initial density maximum. Dark red and dark blue colors denote saturation of the color map. The individual plots are labeled by model. The plot on the extreme right shows the inner region of the KDE plot with $r < 20M$ where the color scale is saturated in the full KDE plot to the left. Here the linear scale is set to the density maximum of the inner torus.

of the inner torus with increasing black hole spin are especially clear in these figures. A more complete summary of the density evolution is provided by the spacetime diagrams of $\langle \rho \rangle (r, \, t)$ in Figure 5. These diagrams illustrate several key points. First, the density maximum of the initial torus is rapidly eroded away from the inside as accretion begins. This density maximum is effectively gone by $t \simeq 3$–5 orbits as matter is redistributed within the disk by the outward transport of angular momentum. Second, one can see the development of the inner torus as a density maximum in the inner disk, fed by accretion from larger radii. The overall accretion is marked by intermittent maxima that appear as a series of leftward-traveling yellow-gray streams.

The distribution of gas pressure $\langle p \rangle (r)$ at late time is similar to that of the density for all models. Of particular interest is the relative distribution of gas and magnetic pressures. Figure 6 shows the late-time, azimuthally averaged value in model KD0 of gas (*left*), magnetic (*middle*), and total pressure (*right*). The total pressure distribution is smooth; the contours are disk-shaped outside the centrifugal barrier, where angular momentum plays a role in the gasdynamics, and are spherically symmetric inside the funnel where the

angular momentum is effectively zero. Comparison of magnetic and gas pressure with the total pressure shows that gas pressure dominates inside the disk, magnetic pressure dominates inside the funnel and in the plunging region, and both contribute on comparable terms within the coronal envelope.

Figure 7 shows gas and magnetic pressure time histories at the radius of the initial gas pressure maximum. As with density, gas pressure at this location decreases to a lower late-time mean value once sustained turbulence is established. Magnetic pressure, $\langle P_{\mathrm{mag}} \rangle$, follows a different course. The magnetic field is initially weak and concentrated at the gas pressure maximum. As the magnetic field is amplified by shearing and the MRI, the radius of the magnetic pressure maximum migrates inward with the accreting matter. There is a brief period, when the MRI saturates, when the magnetic pressure exceeds the gas pressure at the location of the initial gas pressure maximum. But in the late-time quasi–steady state of all four models, gas pressure dominates over magnetic pressure in the main disk.

Another view of the pressure distribution within the models is provided by Figure 8, which shows the ratio of
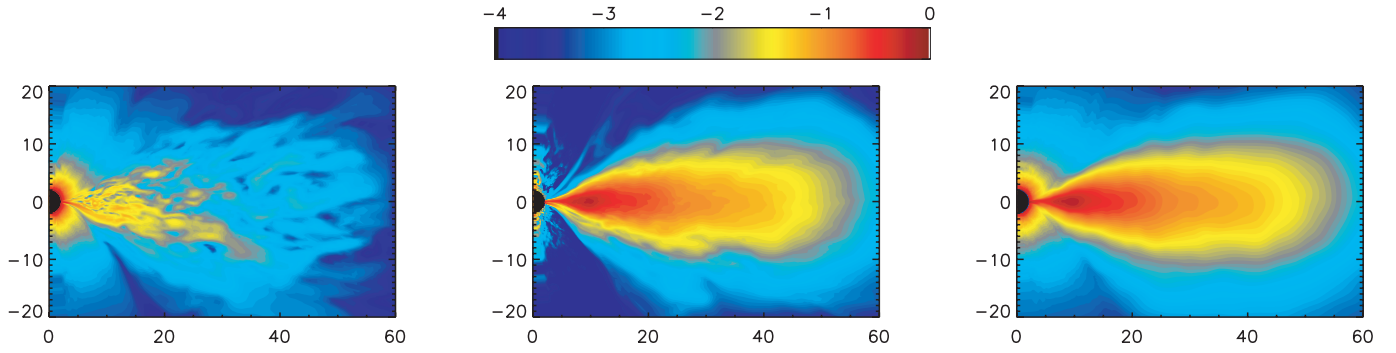
Fig. 6.—Plots of the azimuthally averaged (*left*) magnetic, (*middle*) gas, and (*right*) total pressure for high-resolution model KD0 at $t = 10$ orbits. Pressure is normalized to maximum total pressure and scaled logarithmically, as shown in the color bar.

magnetic to gas pressure, β^{-1}, for each of the high-resolution models. The color scale is centered on $\beta^{-1} = 1$ and shows that the main disk is gas pressure dominated, while in the funnel the converse is true. The coronal envelope stands out in the graph as a region where the gas and magnetic pressures are comparable but not uniformly distributed; more will be said about this in § 3.2.

Full spacetime diagrams of the pressure (not shown) reveal high-frequency waves throughout the disk, especially in models KDP and KDE. The generation of pressure waves seems to be a natural consequence of the turbulence within the disk. The most prominent of these waves seem to occur at frequencies comparable to that of the accretion streams undergoing the final plunge into the black hole. They originate near the point where the flow begins to switch from turbulence-dominated to plunging inflow, a location defined as the turbulence edge in KH02. The pressure waves are common to MRI turbulence and have been seen in many previous simulations. Comparable waves were seen in the previous fully relativistic models of DH03b, as well as the pseudo-Newtonian simulations of HK01 and HK02 (see, e.g., Fig. 9 of HK01). However, with the increased spatial and temporal resolution of the KD models, a greater wealth of detail is now available.

One of the most important dynamical properties of an accretion disk is the overall distribution of angular momentum. Figure 9 shows density-weighted specific angular momentum histories $\langle l \rangle = \langle \rho l \rangle / \langle \rho \rangle$ for the four models. The KD models begin with a radial distribution of specific angular momentum that is slightly shallower than Keplerian, shown here as a thin line. The late-time angular momentum profiles are shown as thick lines, and, for reference, the dashed lines depict $l_{\mathrm{Kep}}(r, a)$, the Keplerian distribution for test particles. Since the models are initialized with a nearly

Keplerian profile, the overall change in $l(r)$ is less dramatic than for the SF models of DH03b. However, the final state in the main disk is similar to the one found in these models, as well as to the final state found in the pseudo-Newtonian simulations of HK01 and HK02, namely, a nearly Keplerian slope with a slightly sub-Keplerian value that rises to very close to the Keplerian value near r_{ms}. Inside the main disk, contours of constant Ω are nearly vertical; in other words, the matter is very close to rotating on cylinders. In all models, the profile continues to decrease smoothly past r_{ms}.

3.2. *Coronal Envelope*

The coronal envelope extends outward from the surface of the disk to the outer boundary of the computational domain and is bounded on the inside by the centrifugal funnel. The gas in this region has low density (Fig. 2) but retains substantial specific angular momentum. As noted in § 3.1, the overall magnetic pressure in the coronal envelope is comparable to the gas pressure ($\beta \sim 1$), although typically the magnetic field is not uniformly distributed in the coronal envelope. There are regions that are more or less magnetized, with β ranging from ≈ 0.3 to 3. As a general rule, the main body of the disk is gas pressure dominated and the funnel region is magnetically dominated, so plots of β provide a useful means of visualizing the coronal envelope (Fig. 8).

The coronal envelope features larger scale, more regular radial motions than the main disk, which is dominated by turbulence. These motions are most clearly visible in animations of poloidal slices of gas density, where gas is seen to blow back from the inner regions of the disk out along the disk surface. It is this ouflowing matter from the disk that
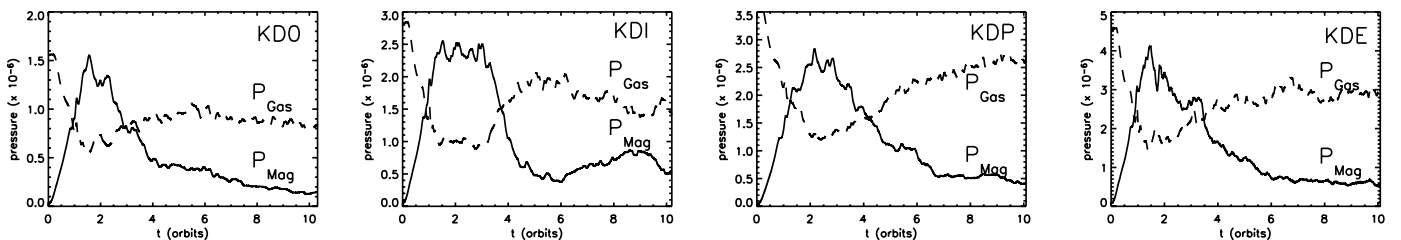

Fig. 7.—Gas and magnetic pressure history, $\langle P_{\mathrm{gas}} \rangle(t)$ and $\langle P_{\mathrm{mag}} \rangle(t)$, at the location of the initial pressure maximum for the high-resolution models. Pressure is given in code units for all four models, allowing cross-comparison of values. The individual plots are labeled by model.
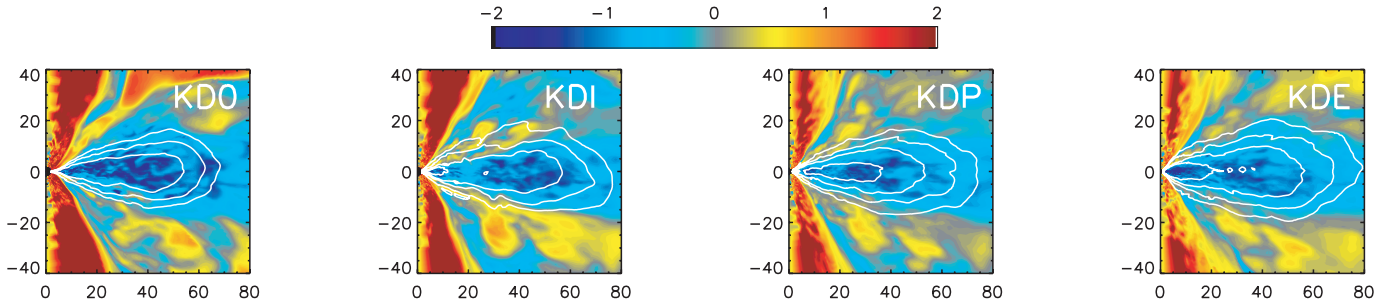
Fig. 8.—Color contours of the ratio of azimuthally averaged magnetic to gas pressure, P_{mag}/P_{gas}, for high-resolution models at $t = 10$ orbits. The scale is logarithmic and is the same for all panels; the color maps saturate in the axial funnel. The body of the accretion disk is identified with overlaid density contours at 10^{-2}, $10^{-1.5}$, 10^{-1}, and $10^{-0.5}$ of $\rho_{max}(t = 0)$. The individual plots are labeled by model.

fills the coronal envelope, and this outflow appears to be a general outcome of turbulence-driven accretion (HB02). The matter outflow tends to keep the gas and magnetic pressures roughly comparable in the corona. This result is in contrast to that of Miller & Stone (2000), who carried out local simulations of a stratified isothermal disk. They found strong magnetic fields, very weak matter outflow, and very small β-values in the corona. Figure 10 shows the azimuthal average of radial mass flux time-averaged over the 10th orbit for each of the high-resolution models. The range of the color maps is chosen for each model to emphasize the radial motions in the coronal envelope and the funnel-wall jet. The color map saturates in the main disk body, where turbulent fluctuations dominate. The figure shows that although the outflow remains irregular even in the coronal envelope, its coherence length is larger than in the disk body. In all four models, the radial flux in the coronal envelope is strongest near the surface of the disk and seems to originate at radii greater than $r \simeq 10M$–$20M$, with a tendency for the point of origin to move inward with increasing a/M. Note that there is a key difference between the outward coronal flows and the funnel-wall jets: the former are bound, while the latter are unbound ($-hU_t > 1$); in a global sense, the coronal flow is therefore more circulatory than consistently outward.

Plots of the magnetic field structure in the coronal envelope (not shown) also reveal a more regular structure in the magnetic field than is the case in the disk body but a less regular structure than is found in the funnel-wall jet or the axial funnel.

3.3. *Inner Torus and Plunging Region*

An important objective for these numerical studies is to investigate the nature of the inner edge of a black hole accretion disk. The inner disk consists of two regions, which we have labeled the "inner torus" and the "plunging region." The inner torus is located where the accretion flow attains a local pressure maximum just outside the marginally stable orbit. In all four models, this location is near $r \approx 1.6r_{ms}$. Detailed time histories of average density (Fig. 5) show that the inner torus is a time-varying structure that mediates the accretion and outflow in its vicinity. Figure 4 shows that the density rises in a relatively continuous (though time variable) way from the disk body to the density maximum marking the inner torus and then falls sharply toward smaller radii. It is the region inside the inner torus and extending into the plunging region that contains the various "inner edges" defined by KH02. These are the locations where turbulence gives way to streaming flow, the disk becomes optically thin, significant local radiation ceases, and dynamical contact with the outer flow can no longer be maintained.

The spacetime diagrams of density in Figure 5 provide a good deal of information on the dynamical behavior of the inner torus. Clearly visible in the plots are small-scale frequent accretion events into the black hole from the inner edge of the inner torus. When accretion from larger radii is not sufficient to immediately resupply the inner torus after such an accretion event, the density in the inner torus is greatly reduced. This can be seen from $t \simeq 3$ to 6 and after $t \simeq 8.5$ in model KD0, from $t \simeq 5$ to 7 in model KDI, and from $t \simeq 7.5$ to 8.3 in model KDP. The inner torus in model KDE seems to grow progressively with time and is at its peak at the end of the simulation, which suggests that the inner region in this model has not attained a quasi–steady state even at this late time.

Although the main body of the disk remains gas pressure dominated at late time (Fig. 7), the magnetic pressure becomes increasingly significant at small radius in all the
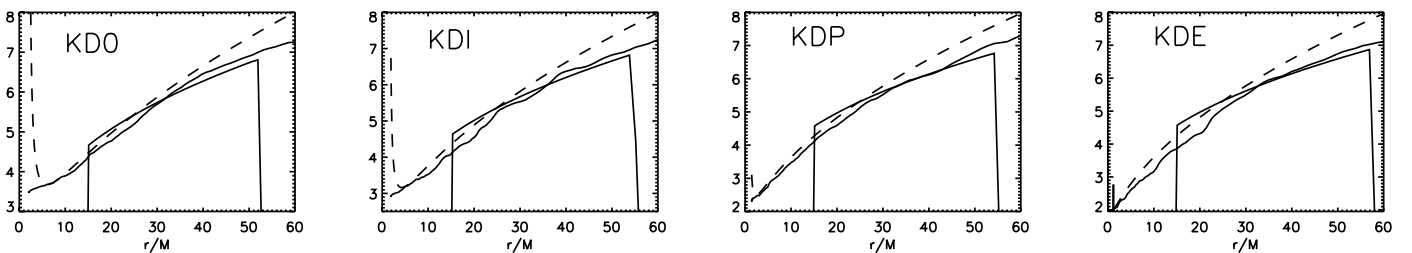

Fig. 9.—Specific angular momentum $\langle l \rangle$ as a function of radius at $t = 0$ (*thin line*) and at $t = 10.0$ orbits (*thick line*). The individual plots are labeled by model. In each case the Keplerian distribution for a test particle, $l_{Kep}(r, a)$, is shown as a dashed line.

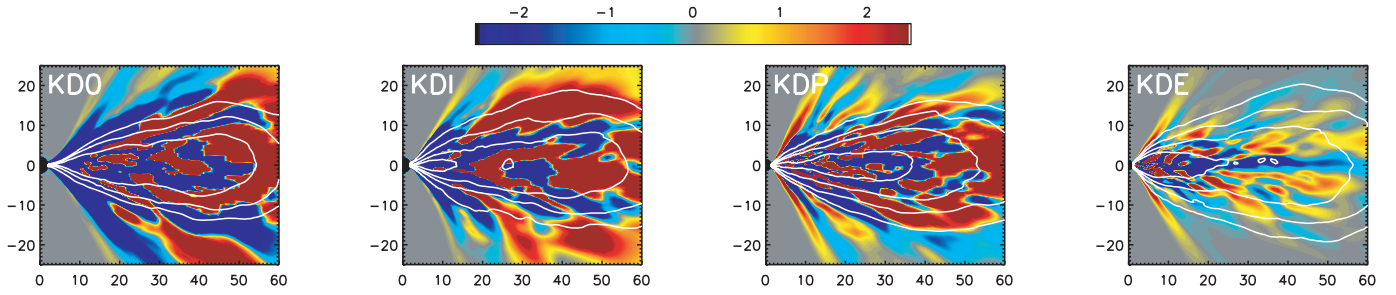FIG. 10.—Color contours of the azimuthally averaged mass flux (ρU^r), time-averaged over the 10th orbit for the four high-resolution models. In each plot the color scale is set to emphasize the outflows in the coronal envelope and the funnel-wall jet; the color scale is multiplied by 10^{-7} for KD0, 10^{-6} for KDI and KDP, and 10^{-5} for KDE. The main body of the disk is indicated by density contours of 10^{-2}, $10^{-1.5}$, 10^{-1}, and $10^{-0.5}$ in units with $\rho_{max}(t=0) = 1$. The individual plots are labeled by model.

models. Figure 11 shows gas and magnetic pressure histories at the inner radial boundary. Because gas pressure is largely confined to the equatorial plane, the shell-integrated values of gas pressure reflect conditions in this region. As for magnetic pressure, it is distributed nearly spherically at small radii, so shell-integrated values of magnetic pressure show roughly a factor of 2 enhancement over typical values in the equatorial plane because of this more extended distribution. The magnetic pressure clearly dominates in models KD0 and KDI, but magnetic and gas pressure are comparable in models KDP and KDE. In part, the difference is due to the relative location of the inner radial grid boundary with respect to the marginally stable orbit; the marginally stable orbit is comparatively closer to the inner boundary in the higher black hole spin models. Between r_{ms} and the horizon, the flow accelerates inward, and the magnetic field evolves primarily by flux freezing. The net result is an increase in magnetic pressure relative to the gas pressure. The larger ratio of magnetic to gas pressure in models KD0 and KDI may be at least partially a consequence of the greater separation between r_{ms} and the inner boundary.

As discussed in KH02, there are several possible ways to mark the inner edge of a black hole accretion disk. One of these is the turbulence edge, the point where the flow makes the transition from turbulence-dominated to plunging inflow past the marginally stable orbit. One indicator of this edge is the point where the radial infall velocity begins to climb with decreasing r. Figure 12 shows the radial velocity profile, obtained from the history ratio $\langle \rho U^r \rangle / \langle \rho \rangle$ and plotted as a function of r/r_{ms}. This plot clearly shows the transition to a smooth accelerating inflow past the marginally stable orbit in all four models. The velocity begins to increase inside about $2r_{ms}$, much as it does in the pseudo-Newtonian calculation (see Fig. 3 of KH02).

One motivation for the pseudo-Newtonian simulations of HK01 and HK02 was to investigate the degree to which magnetic stress continues within the plunging region inside the marginally stable orbit. Here we also see evidence for this phenomenon. Figure 13 shows the density-weighted shell average of hU_ϕ in the models along with the value of $U_\phi(r)$ for circular particle orbits in the equatorial plane. The KD0 and KDI models have the most coordinate distance between r_{ms} and the inner grid boundary, and they show the effect most clearly: hU_ϕ continues to decline with an almost constant slope. The total additional decrease is modest but does demonstrate the continuing role of the magnetic stresses even inside the plunging region. In a subsequent paper we study in greater detail the magnitude of stresses connecting the plunging region to the disk outside r_{ms}.

Inside the disk the instantaneous accretion rate, $\dot{M} = -\langle \rho U^r \rangle$, at any one radius is highly variable. This is a consequence of the turbulence: the velocity fluctuations are significantly larger than the time-averaged radial drift velocity. Averaging over time produces a more representative measure of $\dot{M}$, but even then there are significant variations on longer timescales. For example, animations of the disk density reveal local density maxima that gradually inspiral through the main disk. These maxima account for the prominent accretion events seen in spacetime diagrams. In addition to creating large variations in $\dot{M}$, these episodic events feed bursts of gas into the coronal outflow and funnel-wall jets. Computing the fractional rms accretion rate fluctuation as a function of radius, we find that it is approximately 20% in the region of the inner torus and at smaller radii but rises to values several times greater at radii only twice as large. The details of these fluctuations will be studied in a later paper.
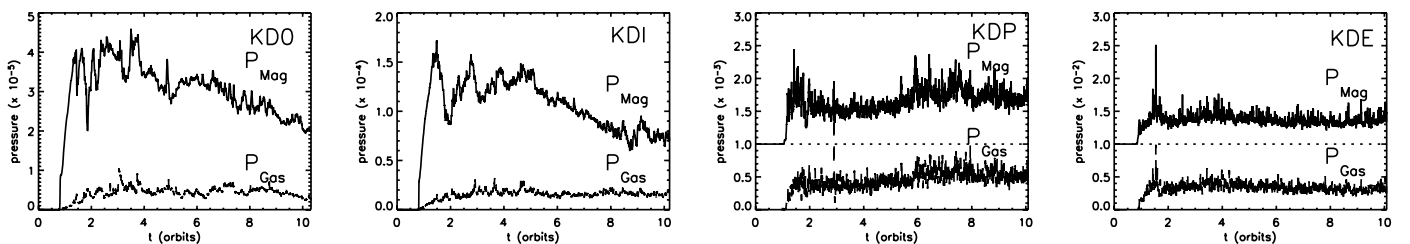

FIG. 11.—Gas and magnetic pressure history, $\langle P_{gas} \rangle$ and $\langle P_{mag} \rangle$, at the inner radial boundary. For clarity, the $\langle P_{mag} \rangle$ curves for models KDP and KDE are shifted vertically by 1.0×10^{-3} and 1.0×10^{-2}, respectively. The individual plots are labeled by model. Pressure is in code units, as in Fig. 7.
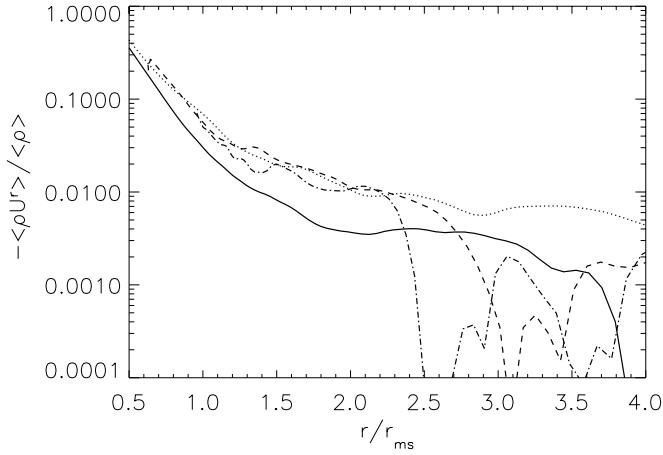
FIG. 12.—Radial velocity profile as a function of r/r_{ms}, computed from $-\langle \rho U^r \rangle / \langle \rho \rangle$ at the end time of the simulation, showing four models, KD0 (*solid line*), KDI (*dotted line*), KDP (*dashed line*), and KDE (*dash-dotted line*).

Some sense of the temporal fluctuations in $\dot{M}$ can be gleaned from Figure 14, which shows the accretion rate through the inner radial boundary as a function of time. The units are the fraction of initial torus mass accreted per M of time. Model KDP shows a slight delay in the onset of accretion compared with the other simulations; this is likely due to the higher β that was used to initialize this model. Following the initial phase in which the MRI is established, the rate of accretion, although variable, seems to settle to a mean value that clearly decreases with increasing black hole spin, a/M. By averaging in time over the second half of the simulations, the mean values are 1.78×10^{-5} for KD0, 1.61×10^{-5} for KDI, 0.82×10^{-5} for KDP, and 0.43×10^{-5} for KDE. Although the initial torus mass is larger for larger a/M, the unnormalized accretion rates for KDP and KDE are still lower than that of KD0. The decrease of accretion rate with increasing a/M was also noted in DH03b, but the connection to black hole spin was not as explicit. In the SF models the ratio $r_{P\,max}/r_{ms}$ varied greatly over the range of
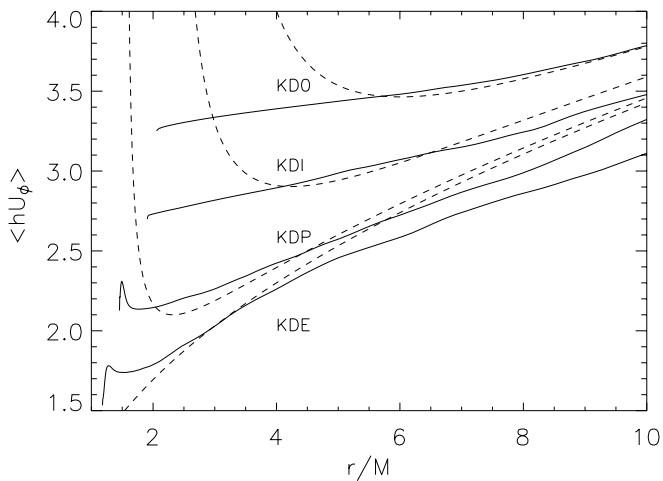

FIG. 13.—Density-weighted shell average of $\langle hU_\phi \rangle = \langle \rho hU_\phi \rangle / \langle \rho \rangle$, time-averaged over the last orbit. The dashed lines are the values of U_ϕ for a circular particle orbit.
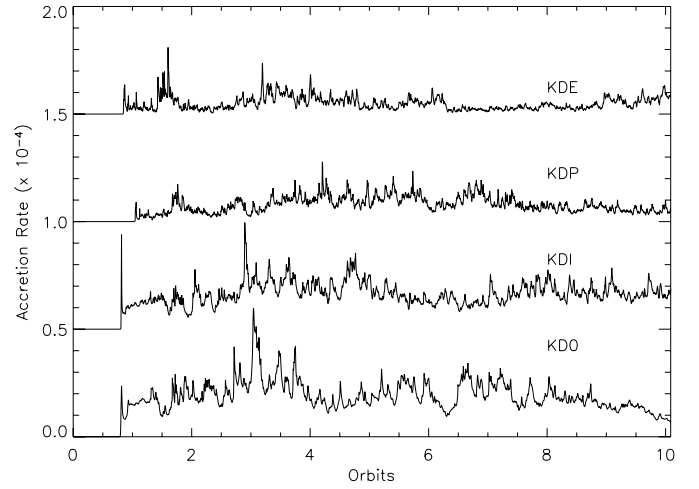

FIG. 14.—Accretion rate $\dot{M} = -\langle \rho U^r \rangle (r_{min})$ through the inner radial boundary as a function of time for the four high-resolution models. The units are the fraction of initial torus mass accreted per unit time M. For clarity, the KDI, KDP, and KDE curves are shifted vertically by 0.5, 1.0, and 1.5×10^{-4}, respectively.

models. Here with the initial pressure maximum farther out, the variation of this ratio is less pronounced across models, yet again the black hole spin is related to the observed accretion rate.

3.4. *Funnel-Wall Jet*

Figure 10 shows the azimuthally averaged radial mass flux, $\overline{\rho U^r}(r, \theta)$, time-averaged over the 10th orbit for each of the high-resolution models. In each plot isodensity contours are added to locate the main body of the disk and the inner torus. These plots show the outflow along the funnel wall, which we have termed the "funnel-wall jet." This jet is particularly prominent in the plots for models KDP and KDE. The funnel-wall jet originates at the boundary between the coronal envelope and the funnel, at the location of the inner torus. In model KD0, where the inner torus is the least prominent, the outflow is extremely weak. As the black hole spin increases, the inner torus shifts inward, becoming increasingly prominent. The base of the jet moves inward with the inner torus; for model KDI, the base of the jet lies just outside the static limit, while in models KDP and KDE, it is inside the ergosphere. In addition, the strength of the jet compared with the radial mass flux in the main disk body also increases with increasing a/M. We find that the jet material moves with a predominantly radial velocity of $\| V \| \approx 0.4c$ in all models; this velocity corresponds to the orbital velocity (V^ϕ) at the launch point of the jet.

The property distinguishing the jet is that the outflowing material within it is unbound, i.e., $-hU_t > 1$. For purposes of a preliminary examination of jet properties, we have studied the jet in model KDP in greater detail and found that the sum of the forces acting on it at large r are decelerative (gravitational). This suggests that the jet is driven impulsively at or near the launch points and that its subsequent motion is ballistic.

Animations of the near-hole region reveal that the jet is not a uniform outflow but is driven in episodic bursts that appear at a frequency comparable to that of the accretion streams that feed the inner torus. To illustrate this,
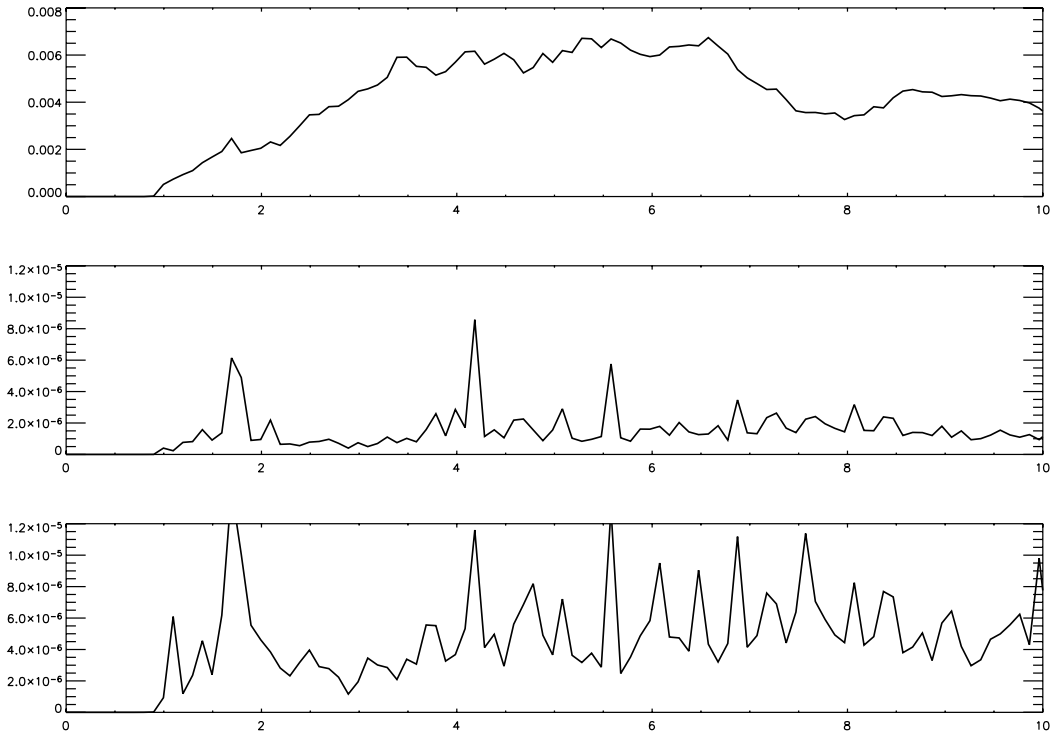
FIG. 15.—Rest mass (as a fraction of total disk mass) in the inner torus, defined as mass inside $r = 6M$ (*top*), and in the funnel-wall jet inside $r < 5M$ (*middle*), and inside $r < 10M$ (*bottom*), as a function of time for model KDP. The data for this plot were extracted from the periodic dumps of the code variables taken every $80M$ in time. The jet is defined as material that is both unbound and outbound (see text).

Figure 15 shows a series of restricted rest-mass histories ($[\rho U^t]$) for model KDP. The top curve shows the total rest mass within the inner torus as a function of time (as a fraction of the initial disk rest mass). The rest mass of the inner torus is computed by restricting $[\rho U^t]$ to $r < 6M$. The two curves below this show the fraction of rest mass in the jets for $r < 5M$ and $r < 10M$. The mass in the jet is extracted from the numerical data by using two criteria: gas deemed to be in the jet is unbound, $-hU_t > 1$, and outbound, $\rho U^r > (\rho U^r)_{\min} > 0$, where $(\rho U^r)_{\min}$ is a mass flux threshold chosen to exclude the more tenuous funnel outflow. The cut was set at 0.5% of the maximum instantaneous unbound mass flux.

Figure 15 shows a steady growth of the mass of the inner torus from $t \simeq 1$ to 3.5 orbits, followed by a decline from $t \simeq 7.5$ to 8.3 orbits. This behavior can also be seen in the spacetime diagram, Figure 5. Figure 15 shows that significant mass is injected into the jet inside $r < 5M$ at only three instants, $t \simeq 1.8$, 4.2, and 5.6 orbits. These features occur just after local, albeit small, upsurges in inner torus mass. They also seem to coincide with accretion events from the inner torus into the black hole (Fig. 5). At other times, the $r < 5M$ curve suggests that matter is fed episodically at a low level near the origin of the jet. It appears, however, that a greater amount of matter is injected into the jet for r between $5M$ and $10M$ (*bottom curve*). The large spike in mass at $t \simeq 1.2$ orbits seen in the bottom curve is a feature related to the outflows that occur during the initial inflow of material from the torus; the funnel-wall jet is not yet established at this time. Together, the two jet mass curves suggest that, although the jet's origin lies near the black hole, a greater portion of the mass in the jet is injected episodically between $r \approx 5M$ and $10M$. A more extensive analysis of the funnel-wall jet will be presented in a subsequent paper.

3.5. *Axial Funnel*

The funnel is the centrifugally evacuated region near the north and south polar axes. The funnel is magnetically dominated and contains a very tenuous gas, which is predominantly moving outward at relativistic velocities ($V^r \simeq 0.95c$). This thin wind is thermally driven; the tenuous gas is very hot with enthalpy $h \gg 1$. The high temperatures result from shocks driven into the funnel by the accretion disk and the corona. Typical gas densities are above the numerical floor but several orders of magnitude below the density in the main disk body and 1–2 orders of magnitude below that of the funnel-wall jet. The small amount of gas present in the funnel has negligible angular momentum, and the edge of the funnel coincides with a very sharp gradient in specific angular momentum that divides coronal gas from funnel gas. Even though there is vigorous outward transport of angular momentum, the gas in the disk retains more than enough specific angular momentum to be excluded from the funnel. In the KDP and KDE simulations some higher angular momentum gas does reach the region near the axis but only in the region very close to the black hole.

The magnetic field, on the other hand, is not so excluded, and the funnel is filled with a predominantly radial field. Because the gas density levels are low, the Alfvén speeds here are high. The magnetic pressure, however, is not extraordinarily large; even at the base of the funnel ($r \simeq 5M$) it is comparable to P_{gas} at the original torus pressure maximum. As shown in Figure 6, the magnetic pressure is nearly spherically symmetric within the funnel; gas pressure here is negligible. Gas pressure dominates within the turbulent disk and drops abruptly across the funnel wall, but the total pressure is smooth and continuous.

TABLE 2
Conserved Quantities in Low- and High-Resolution Models

Model	M_0	M_f	ΔM_i	ΔM_o	$\Delta M_i/M_0$	E_0	E_f	ΔE_i	ΔE_o	L_0	L_f	ΔL_i	ΔL_o	$\Delta L_i/\Delta M_i$
KD0lr	156	140	13.9	0.93	0.089	154	138	13.9	0.99	902	847	44.0	4.42	3.17
KD0	156	130	21.6	1.10	0.138	154	129	20.7	1.17	902	817	68.8	5.66	3.19
KDIlr	258	232	19.7	3.45	0.076	255	229	20.1	4.07	1488	1407	51.8	20.6	2.63
KDI	258	219	31.5	2.82	0.122	255	217	30.5	3.65	1489	1378	82.2	16.7	2.61
KDPlr	291	277	10.7	1.57	0.037	286	273	11.8	2.78	1652	1622	19.3	6.77	1.80
KDP	291	269	16.5	2.48	0.056	286	266	16.2	3.76	1652	1606	21.1	11.6	1.28
KDElr	392	370	8.05	11.8	0.020	386	364	15.6	21.5	2254	2189	−0.88	61.1	−0.11
KDE	392	364	13.8	11.3	0.035	386	359	17.9	21.5	2255	2178	5.79	66.6	0.42

3.6. *Global Quantities*

Aspects of the overall evolution of the disk can be characterized by the time evolution of the total mass (M), energy (E), and momentum (L), computed using equations (19)–(21). Table 2 lists the initial (Q_0) and final (Q_f) values on the grid, as well as the cumulative outflow of each quantity through the inner (ΔQ_i) and outer (ΔQ_o) boundaries, for the four disk models at both low and high resolution. These values were computed every $1M$ in time, corresponding to roughly once every 100 time steps. The boundary fluxes were obtained approximately from state variables at the end of a time step, rather than from the flux values computed by the numerical algorithm within a time step. Since this procedure is approximate, the sum of the outflows and final values on the grid need not match perfectly: for example, the rest-mass totals are low compared with the initial values by about 2%.

Table 2 shows that accretion into the black hole dominates over flow through the outer boundary, except for the KDE models. Generally, it is desirable to avoid significant losses through the outer boundary since such losses could remove dynamically important material from the causal domain of the simulation. Such losses are minimized by locating the outer boundary at large enough radius that the outer part of the disk does not reach it over the course of a typical evolution. The exception to this is model KDE, in which the higher losses through the outer boundary result from the larger relative size of the initial torus.

The largest total rest mass accreted as a fraction of the initial mass is 14% for model KD0. The accreted mass decreases with increasing a/M, and the low-resolution simulations consistently yield a lower accreted mass than their high-resolution counterparts. In the pseudo-Newtonian simulation of HK02, 16.6% of the initial torus mass is accreted in 10 orbits of time at its initial pressure maximum ($R = 20M$). Compared with the SF0 and SFP models of DH03b, the fraction of disk mass accreted into the black hole in the KD models is smaller, even though the KD models are run for a longer absolute time. The SF models feature a strong transient accretion flow during the early evolution of the initially constant angular momentum torus. This contributes to the higher accreted mass in these models.

Over the course of the evolution the average specific energy E/M increases with time as the gas on the grid becomes less bound. The greatest change in average specific energy occurs for the low a/M models, 0.23% for KD0 and 0.25% for KDI. Smaller changes occur for the high a/M models, 0.11% for KDP and 0.01% for KDE. In the last case the loss of less-bound material through the outer boundary

seems to nearly compensate for the inflow of more-bound material into the black hole.

The average specific angular momentum on the grid, L/M, also increases with time. For all models except KDE, more low angular momentum mass has entered the hole than high angular momentum material has exited through the outer boundary. There is considerable variation between values obtained in the high- and low-resolution models of KDP and KDE. In particular, model KDElr shows a negative ΔL_i, which is likely an artifact due to an underresolved plunging region. However, the high-resolution models do show an interesting overall trend: the specific angular momentum accreted into the hole, $\Delta L_i/\Delta M_i$, decreases with increasing a/M compared with the marginally stable value, l_{ms}. On the other hand, the values of $\langle hU_\phi \rangle$ (Fig. 13) are below the marginally stable value of U_ϕ for models KD0 and KDI, in which there is an extended plunging region, but comparable to $(U_\phi)_{ms}$ for models KDP and KDE, where $\langle hU_\phi \rangle \approx 2.1$ and 1.5, respectively. The stresses and fluxes within the plunging regions will be examined in greater detail in a subsequent paper.

4. DISCUSSION

We have computed a set of three-dimensional MHD accretion simulations for a range of Kerr black hole spin parameters. These models are general relativistic versions of previous pseudo-Newtonian simulations (HK01; HK02) that studied the evolution of a torus with a nearly Keplerian angular momentum distribution and weak poloidal loops of magnetic field. The accretion flows are nonradiative and evolve from a fixed amount of initial mass, which increases with increasing a/M. In this paper we present an initial survey of the results, describing the overall structure of the accretion flow that develops. We label and describe a set of five specific features in the accretion flow. These are the turbulent dense main disk body with a roughly constant H/R, the inner disk consisting of an inner torus and a plunging inflow, a magnetized coronal envelope surrounding the disk, a jetlike outflow along the funnel wall, and an evacuated axial funnel.

In our preliminary analysis we are looking for ways in which the spin of the black hole affects the overall evolution. One such effect that immediately emerges is a decrease in the accretion rate into the hole with increasing spin parameter a/M. This was also seen in the previous study of constant-l tori in the Kerr metric (DH03b), in which the role of black hole spin was partially explored, but the issue of accretion rate and its relation to a/M was somewhat obscured by the

choice of initial conditions. The initial tori had inner boundaries that were closer to the black hole than for the tori used here, and the range of spin parameters yielded a substantial variation in the ratio $r_{P\max}/r_{\rm ms}$. In the KD models, the initial tori are located at larger radii compared with $r_{\rm ms}$, and the variation in the ratio of initial pressure maximum to marginally stable orbit is less pronounced. There are several ways that increased black hole spin can influence the accretion rate. One is that the inner torus, located near $r_{\rm ms}$, is thicker and hotter with increasing black hole spin. In the absence of cooling, this high-pressure inner torus could choke off the accretion flow. Another way that the accretion rate could be influenced is through the a/M-dependent shape of the effective potential near $r_{\rm ms}$. A third way, suggested by the large electromagnetic angular momentum flux seen in KDP and KDE, is for magnetic torques driven by the black hole's rotation to supply some of the outward angular momentum flux through the disk body. These dynamical effects will be investigated in greater detail in a subsequent paper.

In all models the accretion rate is highly time- and space-variable, and this, in turn, makes the characteristics of the inner torus vary in time as larger or smaller amounts of gas are brought into the near-hole region from the extended disk. The inner torus therefore exerts an important influence on the accretion flow into the black hole, acting as a temporary reservoir that feeds some matter through the potential "cusp" and into the plunging region while also sending mass outward along the funnel wall. This latter feature, the funnel-wall jet, is launched somewhat sporadically from a point in the coronal envelope above the inner torus. The jet flows outward along the boundary between the coronal envelope and the axial funnel. The intensity of the jet increases with black hole spin, as the origin of the jet moves gradually deeper into the potential well of the black hole.

As in the previous pseudo-Newtonian simulations, we find that significant stress continues to operate well inside the marginally stable orbit. As a result, the angular momentum accreted per unit mass is less than the specific angular momentum of matter following the marginally stable orbit, in contrast to the expectations of the classical Novikov-Thorne model (Novikov & Thorne 1973). When the black hole is rotating relatively slowly or not at all (KDI and KD0), the difference between the accreted $l_{\rm in}$ and $l_{\rm ms}$ is noticeable but modest, $l_{\rm in}/l_{\rm ms} \sim 85\%$. On the other hand, when $a/M = 0.9$ (KDP), the angular momentum per unit mass carried into the hole is about 50% $l_{\rm ms}$, and when $a/M = 0.998$ (KDE), the value is only 20%. While these specific numbers should be regarded with caution, as there is considerable variation with different grid resolution, the trend with increasing a/M seems more robust. In the lower spin simulations (KD0 and KDI), the net angular momentum accreted by the black hole is dominated by the part directly associated with matter (i.e., near the inner boundary $\mathbf{T}_\phi^r \simeq h\rho\mathbf{U}^r\mathbf{U}_\phi$); however, as the spin increases, the angular momentum associated with the magnetic field (i.e., the terms $\|b\|^2\mathbf{U}^r\mathbf{U}_\phi - \mathbf{b}^r\mathbf{b}_\phi$ in the stress tensor) become increasingly important. In fact, most of the reduction in accreted specific angular momentum seen in the higher spin simulations is due to *negative* magnetic angular momentum flux. It is interesting to note that in the KDE simulation, this effect is so strong that there could be spin-down of the black hole (if the background metric were not fixed), as the angular momentum accreted per unit mass is less than the angular momentum per unit mass stored in the black hole.

The models discussed here represent one more step in a program to pursue increasingly realistic simulations of magnetically driven accretion flows in black hole spacetimes. With the availability of significant computing power, spatial resolution is less of a limiting constraint than it was just a few years earlier; however, higher resolution simulations than were carried out here remain necessary to address the issue of numerical convergence. For the present study we have run each model at two resolutions. We see systematic resolution-dependent differences in such quantities as accretion rate through the inner radial boundary and the specific angular momentum and energy of that accretion flow. These models also were run on a restricted azimuthal grid of $\pi/2$. As noted in DH03b, there are differences with a full 2π model, including a reduction in the variability of the accretion rate and an increase in the average accretion rate. Resolution through the main disk body is also a critical issue, since the modes that sustain the MRI must be adequately resolved for turbulence to sustain accretion throughout the simulation. Experiments have shown that the lower resolution (lr) grids used here are near the lower limit in this regard.

While these considerations certainly argue for the desirability of increased resolution, the grids that we have been able to use here have allowed us to probe for the first time some of the time-dependent dynamics of accretion flows down to near the event horizon of rotating black holes, within the limits of the Boyer-Lindquist coordinate system. In subsequent papers in this series we will look more deeply into these models, including looking at the role of stress inside the marginally stable orbit and the apparent influence of black hole spin, as well as investigate more closely the details in the regions of the flow identified here.

REFERENCES

Abramowicz, M., Jaroszyński, M., & Sikora, M. 1978, A&A, 63, 221
Armitage, P. J., & Reynolds, C. S. 2003, MNRAS, 341, 1041
Armitage, P. J., Reynolds, C. S., & Chiang, J. 2001, ApJ, 548, 868
Balbus, S. A., & Hawley, J. F. 1991, ApJ, 376, 214
———. 1998, Rev. Mod. Phys., 70, 1
Bardeen, J. M., Press, W. H., & Teukolsky, S. A. 1972, ApJ, 178, 347
Chakrabarti, S. K. 1985, ApJ, 288, 1

De Villiers, J. P., & Hawley, J. F. 2003a, ApJ, 589, 458 (DH03a)
———. 2003b, ApJ, 592, 1060 (DH03b)
Gammie, C. F. 1999, ApJ, 522, L57
Hawley, J. F. 2000, ApJ, 528, 462 (H00)
———. 2001, ApJ, 554, 534
Hawley, J. F., & Balbus, S. A. 2002, ApJ, 573, 738 (HB02)
Hawley, J. F., & Krolik, J. H. 2001, ApJ, 548, 348 (HK01)
———. 2002, ApJ, 566, 164 (HK02)

Hawley, J. F., Smarr, L. L., & Wilson, J. R. 1984, ApJ, 277, 296
Krolik, J. H. 1999, ApJ, 515, L73
Krolik, J. H., & Hawley, J. F. 2002, ApJ, 573, 754 (KH02)
Machida, M., & Matsumoto, R. 2003, ApJ, 585, 429
Miller, K. A., & Stone, J. M. 2000, ApJ, 534, 398
Novikov, I. D., & Thorne, K. S. 1973, in Black Holes: Les Astres Occlus, ed. C. de Witt & B. de Witt (New York: Gordon & Breach), 344
Page, D. N., & Thorne, K. S. 1974, ApJ, 191, 499
Papaloizou, J. C. B., & Nelson, R. 2003, MNRAS, 339, 983
Steinacker, A., & Papaloizou, J. C. B. 2002, ApJ, 571, 413